DOI:
10.1109/TBME.2018.2849648

Document Version
Peer reviewed version

A Multi-Threshold Iterative DBIM-Based Algorithm for the Imaging of Heterogeneous Breast Tissues

Michele Ambrosanio, *Member, IEEE*, Panagiotis Kosmas, *Senior Member, IEEE*, and Vito Pascazio, *Senior Member, IEEE*

***Abstract*—Microwave imaging (MWI) represents a well-known tool for quantitatively retrieving unknown objects in a non-destructive way. Microwave radiation is non-ionizing, which suggests that MWI can be also attractive for medical diagnostics applications. This work proposes a novel MWI multi-frequency technique, which combines compressive sensing (CS) with the well-known distorted Born iterative method (DBIM). CS strategies are emerging as a promising tool in MWI applications, which can improve reconstruction quality and/or reduce the number of data samples. The proposed approach is based on iterative shrinkage thresholding algorithm (ISTA), which has been modified to include an automatic and adaptive selection of multi-threshold values. This adaptive multi-threshold ISTA (AMTISTA) implementation is applied in reconstruction of two-dimensional (2-D) numerical heterogeneous breast phantoms, where it outperforms the standard thresholding implementation. We show that our approach is also successful in three-dimensional (3-D) simulations of a realistic imaging experiment, despite the mismatch between the data and our algorithm's forward model. These results suggest that the proposed algorithm is a promising tool for medical MWI applications.**

***Index Terms*—Microwave imaging, electromagnetic inverse scattering, distorted Born iterative method (DBIM), compressive sensing (CS), medical imaging.**

I. Introduction

Electromagnetic (EM) inverse scattering theory relies on a great variety of algorithms which can be employed to compute images of an inaccessible domain using EM signals [1]. At microwave frequencies, various imaging algorithms exist for a wide range of applications in the biomedical field, including brain stroke monitoring [2], evaluation of bones' health [3], and breast cancer imaging [4]. More recently, various groups have also been considering new microwave imaging (MWI) and therapy applications, such as MWI and hyperthermia treatment of cancer by means of magnetic nanoparticles [5].

Microwave breast cancer imaging (BCI) research includes two families of techniques: tomographic and radar-based. Tomographic algorithms aims to produce a full image of the region under test, while radar-based methods aim to identify a pathology within a region without inferring a complete image of the breast [6], [7]. Tomographic techniques for breast imaging have been applied to both treatment monitoring [8], [9] as well as breast cancer detection [10]–[12].

A popular approach in EM microwave tomography is based on the distorted Born iterative method (DBIM) [13]–[15], which uses a succession of linear approximations to estimate both morphological and dielectric features of the reconstruction domain. In this work, the linear system of equations at each DBIM iteration is solved by using an iterative method based on adaptive shrinkage soft thresholding. This approach belongs to a wider class of methods based on compressed sensing (CS) theory [16]–[20].

CS methods rely on a L^1-minimization procedure such as the basis pursuit [21] or the least absolute shrinkage and selection operator (LASSO) [22], [23], which is based on convex optimization. Orthogonal matching pursuit (OMP) [24] builds the support of the reconstructed sparse vector by adding iteratively one index per time at the current support at each iteration. OMP is computationally more efficient compared to basis pursuit and LASSO, at the cost of recovery performance. Bayesian approaches have also been successfully applied to both single and multi-frequency MWI algorithms [25]–[27].

Thresholding techniques, such as iterative hard thresholding (IHT) proposed in [28], [29] and the modified version of the iterative shrinkage thresholding algorithm (ISTA) [30] proposed in this paper, can be viewed as a compromise in the trade-off between computational efficiency and recovery accuracy. They set the profile support in one step by choosing coefficients which maximize the correlations between the propagation and scattering matrix and the unknown profile. At each iteration, the application of either soft or hard thresholding enforces sparsity on the unknown vector. This sparsity promotion [31] in the solution of the under-determined linear problem can improve the convergence of the DBIM algorithm, for example in applications related to microwave breast cancer imaging (BCI) [32], [33].

As for all the inversion strategies, the choice of the regularization parameter still represents an issue. In the ISTA framework, the thresholding operation depends on this selection and can provide very different results. Generally, the use of some a priori information, like the level of sparsity of the considered signal or the noise level, is required for a proper setting of the regularization strategy. Therefore, the use of an efficient selection criterion for fixing the regularization parameter is of great interest in the scientific community.

This work proposes a novel ISTA implementation as the linear solver of the DBIM, which results in a robust and flexible approach to microwave tomography. The algorithm

M. Ambrosanio and V. Pascazio are with the Department of Engineering, University of Napoli Parthenope, 80143, Napoli, Italy and with Consorzio Nazionale Interuniversitario per le Telecomunicazioni (CNIT), UdR of Napoli Parthenope.

P. Kosmas is with Faculty of Natural and Mathematical Sciences, King's College London, WC2R 2LS, London, UK, and with MediWiSe — Medical Wireless Sensing Ltd, 42 New Road, London E1 2AX, UK.

e-mail:{michele.ambrosanio, vito.pascazio}@uniparthenope.it, panagiotis.kosmas@kcl.ac.uk

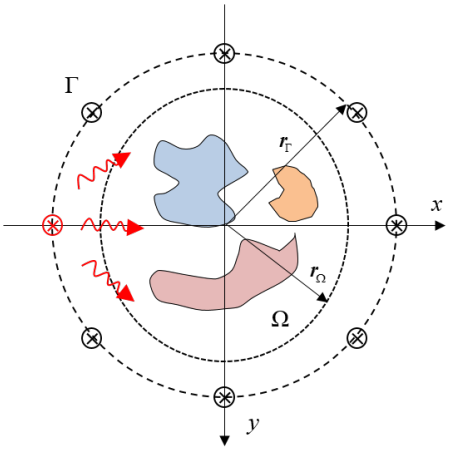

Fig. 1. Multiview-multistatic microwave imaging setup. Γ represents the measuring contour on which all the probes (transmitters and receivers) are located, while Ω is the imaging domain filled with a matching medium. The red circle refers to the transmitting probe and the black ones to the receivers (only one transmitter per time is active).

implements a multi-threshold strategy which can estimate more efficiently the unknown objects (frequency dependent) complex permittivity. To improve the algorithms robustness, we implement an automatic threshold selection process, which is shown to be effective for numerical breast phantoms of different inhomogeneity profiles.

The remainder of the paper is organised as follows: Section II reviews the mathematical formulation of the inverse problem at hand, while Section III details our proposed approach. Numerical results presented in Section IV show that the proposed method outperforms the standard sparsity-based version of ISTA for microwave breast imaging. Finally, we present a summary with conclusions and possible work in Section V.

II. Mathematical Formulation

In the following, a simplified two-dimensional geometry is considered by using transverse-magnetic (TM) electric fields generated by z-oriented current wires, employed both as transmitting and receiving antennas. All the probes are located on a measurement contour Γ which is included in the computational domain and contains the imaging domain, realizing a multiview-multistatic configuration. The scattered field is collected at the receivers locations along the measuring contour Γ (see Fig. 1). Inversion is carried out by exploiting the well-known distorted Born approximation [15], [34]–[40], which linearizes the full-wave scattering equation in a linear version by replacing the total field E_t with the known "incident" field E_i, i.e. the electric field evaluated for the chosen complex permittivity assumed as background.

A. Overview of the DBIM formulation

The k-th iteration of the DBIM inversion procedure can be expressed mathematically as:

$$\begin{aligned}\Delta E_s^{(k)}(\mathbf{r}_{Rx},\mathbf{r}_{Tx},\omega) &= E_t(\mathbf{r}_{Rx},\mathbf{r}_{Tx},\omega) - E_i^{(k)}(\mathbf{r}_{Rx},\mathbf{r}_{Tx},\omega)\\ &\approx \omega^2\mu \iint_\Omega G^{(k)}(\mathbf{r}_{Rx},\mathbf{r}',\omega)\varrho^{(k)}(\mathbf{r}',\omega)E_i^{(k)}(\mathbf{r}',\mathbf{r}_{Tx},\omega)dr',\\ &\mathbf{r}_{Tx},\mathbf{r}_{Rx}\in\Gamma,\quad \mathbf{r}'\in\Omega.\end{aligned} \tag{1}$$

in which $\varrho^{(k)}(\mathbf{r}',\omega) = \epsilon^{(k)}(\mathbf{r}',\omega) - \epsilon_b^{(k)}(\mathbf{r}',\omega)$ represents the difference between targets' complex permittivity and that of the background (the "contrast function"), and $\mathbf{r}_{Tx}$ and $\mathbf{r}_{Rx}$ are vectors pointing at transmitter and receiver locations. The function $G^{(k)}$ represents the inhomogeneous Green's function, i.e. the impulse response of the system at the k-th DBIM iteration. After the linear inversion, the complex permittivity estimation is improved by adding the new update to the background permittivity of previous step, i.e. $\epsilon_b^{(k+1)}(\mathbf{r},\omega) = \epsilon_b^{(k)}(\mathbf{r},\omega) + \varrho^{(k)}(\mathbf{r},\omega) = \epsilon^{(k)}(\mathbf{r},\omega)$.

Equation (1) can be re-arranged as function of the contrast $\varrho^{(k)}$, leading to a matrix equation [41], [42]:

$$\mathbf{A}^{(k)}(\omega)\boldsymbol{\varrho}^{(k)}(\omega) = \Delta\tilde{\mathbf{E}}_s^{(k)}(\omega), \tag{2}$$

in which $\mathbf{A}^{(k)}(\omega)$ is the matrix which relates the data (the scattered field samples $\Delta\tilde{\mathbf{E}}_s^{(k)}(\omega)$) to the unknowns (the contrast function samples $\boldsymbol{\varrho}^{(k)}$) at the single frequency ω, where the dependence on $\mathbf{r}$ has been neglected and $\Delta\tilde{\mathbf{E}}_s^{(k)}(\omega)$ represents the noisy measured version of $\Delta\mathbf{E}_s^{(k)}(\omega)$.

Our DBIM implementation relies on a finite difference time domain (FDTD) forward solver and the use of a Debye model to capture the dependence of breast tissues with frequency:

$$\epsilon_r(\mathbf{r},\omega) = \epsilon_\infty(\mathbf{r}) + \frac{\Delta\epsilon(\mathbf{r})}{1+j\omega\tau} + \frac{\sigma_s(\mathbf{r})}{j\omega\epsilon_0}, \tag{3}$$

in which the quantities $\epsilon_\infty(\mathbf{r})$, $\Delta\epsilon(\mathbf{r})$ and $\sigma_s(\mathbf{r})$ are the unknown parameters of the Debye model to be determined. As in previous work [14], we assume that the relaxation time constant "τ" is known and invariant with position, equal to 17.5 picosecond. This is a reasonable assumption since this constant does not vary extensively across the different biological tissues of the breast [43]–[45].

The use of Debye model described by (3) allows a multi-frequency implementation of the DBIM, which can increase independent information content [46], and thus enhance the reconstruction capabilities of MWI algorithms. Using this Debye model, the matrix equation (2) is transformed to (4), which describes the linear problem at each iteration of the multi-frequency DBIM algorithm.

B. ISTA approach for solving the linear problem

Previous work has shown that sparsity can represent an efficient way to solve the linear inverse problem in MWI via the DBIM [28], [29]. Sparsity refers to the number of non-zero coefficients of the unknown vector, which can be captured by the so-called L^0-norm. Unfortunately, since all the L^0-norm minimization procedures represent NP-hard problems,

$$\overbrace{\begin{bmatrix} Re\{\mathbf{A}^{(k)}(\omega_1)\} & \frac{Re\{\mathbf{A}^{(k)}(\omega_1)\}+\omega_1\tau Im\{\mathbf{A}^{(k)}(\omega_1)\}}{1+(\omega_1\tau)^2} & \omega_1\omega_1^{-1} Im\{\mathbf{A}^{(k)}(\omega_1)\} \\ Im\{\mathbf{A}^{(k)}(\omega_1)\} & \frac{Im\{\mathbf{A}^{(k)}(\omega_1)\}-\omega_1\tau Re\{\mathbf{A}^{(k)}(\omega_1)\}}{1+(\omega_1\tau)^2} & -\omega_1\omega_1^{-1} Re\{\mathbf{A}^{(k)}(\omega_1)\} \\ Re\{\mathbf{A}^{(k)}(\omega_2)\} & \frac{Re\{\mathbf{A}^{(k)}(\omega_2)\}+\omega_2\tau Im\{\mathbf{A}^{(k)}(\omega_2)\}}{1+(\omega_2\tau)^2} & \omega_1\omega_2^{-1} Im\{\mathbf{A}^{(k)}(\omega_2)\} \\ Im\{\mathbf{A}^{(k)}(\omega_2)\} & \frac{Im\{\mathbf{A}^{(k)}(\omega_2)\}-\omega_2\tau Re\{\mathbf{A}^{(k)}(\omega_2)\}}{1+(\omega_2\tau)^2} & -\omega_1\omega_2^{-1} Re\{\mathbf{A}^{(k)}(\omega_2)\} \\ \cdots & \cdots & \cdots \\ \cdots & \cdots & \cdots \\ Re\{\mathbf{A}^{(k)}(\omega_F)\} & \frac{Re\{\mathbf{A}^{(k)}(\omega_F)\}+\omega_F\tau Im\{\mathbf{A}^{(k)}(\omega_F)\}}{1+(\omega_F\tau)^2} & \omega_1\omega_F^{-1} Im\{\mathbf{A}^{(k)}(\omega_F)\} \\ Im\{\mathbf{A}^{(k)}(\omega_F)\} & \frac{Im\{\mathbf{A}^{(k)}(\omega_F)\}-\omega_F\tau Re\{\mathbf{A}^{(k)}(\omega_F)\}}{1+(\omega_F\tau)^2} & -\omega_1\omega_F^{-1} Re\{\mathbf{A}^{(k)}(\omega_F)\} \end{bmatrix}}^{\mathbf{B}^{(k)}} \overbrace{\begin{bmatrix} \boldsymbol{\epsilon}_\infty^{(k+1)} - \boldsymbol{\epsilon}_\infty^{(k)} \\ \Delta\boldsymbol{\epsilon}^{(k+1)} - \Delta\boldsymbol{\epsilon}^{(k)} \\ \frac{\boldsymbol{\sigma}_s^{(k)} - \boldsymbol{\sigma}^{(k)}}{\omega_1\epsilon_0} \end{bmatrix}}^{\mathbf{x}^{(k)}} = \overbrace{\begin{bmatrix} Re\{\Delta\tilde{\mathbf{E}}_s^{(k)}(\omega_1)\} \\ Im\{\Delta\tilde{\mathbf{E}}_s^{(k)}(\omega_1)\} \\ Re\{\Delta\tilde{\mathbf{E}}_s^{(k)}(\omega_2)\} \\ Im\{\Delta\tilde{\mathbf{E}}_s^{(k)}(\omega_2)\} \\ \cdots \\ \cdots \\ Re\{\Delta\tilde{\mathbf{E}}_s^{(k)}(\omega_F)\} \\ Im\{\Delta\tilde{\mathbf{E}}_s^{(k)}(\omega_F)\} \end{bmatrix}}^{\tilde{\mathbf{y}}^{(k)}} \quad (4)$$

a more computationally tractable version in noisy scenarios is required. Therefore, the considered problem can be driven into a L^1-norm minimization procedure of the type (omitting the ω dependence) [47]:

$$\min \| \mathbf{x}^{(k)} \|_{L^1} \text{ subject to } \| \tilde{\mathbf{y}}^{(k)} - \mathbf{B}^{(k)}\mathbf{x}^{(k)} \|_{L^2}^2 < \delta, \quad (5)$$

in which δ is a small number. In order to solve the problem defined in (5), a possible strategy is represented by ISTA, for which the general step can be written as [30]:

$$\begin{aligned} \mathbf{x}_{(i+1)}^{(k)} = \mathcal{S}_{\lambda\cdot\alpha^{(k)}} \Big(& \mathbf{x}_{(i)}^{(k)} + \\ & + \alpha^{(k)} \left[\mathbf{B}^{(k)}\right]^\dagger \left(\tilde{\mathbf{y}}^{(k)} - \mathbf{B}^{(k)}\mathbf{x}_{(i)}^{(k)}\right) \Big), \\ & i = 1, \cdots, N_{ISTA} \end{aligned} \quad (6)$$

in which $\mathcal{S}_{\lambda\cdot\alpha^{(k)}}$ represents the soft-shrinkage thresholding operator, N_{ISTA} is the number of ISTA iterations (i.e., the inner loop), $\left[\mathbf{B}^{(k)}\right]^\dagger$ denotes the conjugate transpose of the matrix $\mathbf{B}^{(k)}$.

The parameter $\alpha^{(k)}$ represents a convergence parameter which is chosen in the range $\left(0, 2/\mathscr{S}_{max}\left[\mathbf{B}^{(k)}\right]\right)$, in which $\mathscr{S}_{max}\left[\mathbf{B}^{(k)}\right]$ is the largest singular value of the matrix $\mathbf{B}^{(k)}$ [40], [48], and λ is a regularization parameter. The threshold is fixed at $T^{(k)} = \lambda \cdot \alpha^{(k)}$ and its choice does not represent a trivial task, but should be carefully tuned using some a priori information on the signal before getting its recovery.

Many criteria have been proposed for setting the regularization parameter properly. In [21], [49] this parameter is fixed at $\lambda = \sigma\sqrt{2log\,(p)}$, with p cardinality of the considered dictionary and σ the estimated level of noise. Conversely, Fang et al. [50] propose an adaptive threshold along the outer loop of the minimization scheme, i.e. $\lambda^{(k)} = |\mathbf{x}^{(k)}|_s$, with k representing the considered DBIM iteration and $|(\cdot)|_s$ being the absolute value of the s-th non-zero coefficient of $(\cdot)$. Unfortunately, both these criteria require some strong a priori information in order to be set, such as the noise level or the degree of sparsity of the solution.

The methodology proposed in this paper aims at improving the thresholding operation by a proper selection of the regularization parameter without any prior information, enhancing reconstruction performance in the framework of the DBIM-based microwave imaging.

III. The Adaptive Multi-Threshold Shrinkage Thresholding Algorithm (AMTISTA)

A. Methodology and Innovations

The general framework of ISTA approaches is well-known in the optimization literature. It belongs to gradient-based methods and can be related to the proximal forward-backward iterative scheme introduced in [51]–[53]. Among all the different kinds of available thresholds, this paper focuses on the "soft-shrinkage" thresholding, which consists of throwing away all the signal coefficients which are below the threshold value and "rescaling" the remaining coefficients according to a linear mapping. Our algorithm follows this general approach but also implements modifications which can improve DBIM's performance in microwave breast imaging.

In particular, we observe that the vector of unknowns in (4) includes a conductivity term which is much lower in magnitude compared with the permittivity terms, even after rescaling by the factor $\omega_1\epsilon_0$. For this reason, a thresholding algorithm based on the use of three different thresholds is developed in this work. The use of a different threshold for each group of unknowns (multi-threshold) in the Debye model allows us to account for differences in their convergence rate and estimated values (see Fig. 2 for a proof of concept of the multi-threshold idea). The idea of employing multiple thresholds has been proposed previously [54]–[56], but its use within a CS-DBIM framework is proposed here for the first time, to the best of authors' knowledge.

Beyond the multi-threshold concept, the proposed approach is characterized by an adaptive selection of the coefficients based on the previous DBIM iteration. For the previous reasons, this methodology has been named AMTISTA (adaptive multi-threshold iterative shrinkage thresholding algorithm)

Another advantage of the proposed algorithm is its ability to incorporate bounds on Debye parameters as constraints inside the AMTISTA solver. This is more effective than enforcing hard constraints at the end of each DBIM iteration, which can lead the minimization procedure to a deadlock. On the contrary, our proposed approach forces the algorithm *not* to update those pixels which have already reached the *saturation condition*, i.e. all those pixels that exceed the minimum and maximum bounds fixed from the initial a priori information, and treating the linear problem as a constrained optimization procedure.

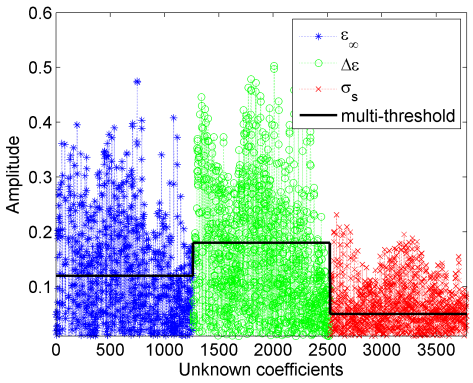

Fig. 2. Proof of concept: plot of the amplitude of the unknown coefficients vector $\mathbf{x}^{(k)}$ at the generic k-th iteration. Each color refers to one of the Debye unknowns (see figure label). The black continuous line illustrates the differences in the thresholds, which motivates our proposed multi-threshold approach.

B. Implementation

Fig. 3 shows a brief sketch of the proposed approach. The scheme consists of two steps, with the first one consisting of a single-frequency reconstruction which results in a low-resolution image. This image is used as initial guess in the second, multi-frequency DBIM reconstruction in order to increase robustness and enhance recovery performance. The first step initial guess assumes only knowledge of the breast external surface (the skin thickness and properties are unknown), which is filled with a homogeneous Debye medium representing average breast tissue ($\epsilon_\infty = 5.76, \quad \Delta\epsilon = 5.51$ and $\sigma_s = 0.08$ S/m).

The inversion scheme starts with a finite difference time domain (FDTD) forward solver with convolution perfectly matched layers (CPML) based on a recursive-convolution technique [57], which are necessary in order to prevent non-physical reflections from outgoing waves for a wide range of incident angles. The employed source is a modulated Gaussian pulse, i.e.:

$$J_z(t) = sin(\omega(t-\Delta)) \cdot e^{-\frac{(t-\Delta)^2}{T_d^2}}, \tag{7}$$

in which $\omega = 2\pi f$, f is the carrier frequency, Δ is the time shift for the impulse start and T_d is proportional to the pulse duration. Eq. (7) describes the current source as a function of time in the source location. Then, the total field evaluated at k-th iteration of the DBIM is compared with the reference data in order to obtain an approximated linear equation (4), which is solved by using a standard Landweber approach [58] without any thresholding. After reaching the convergence at iteration $k = N$, which could be verified when the residual error between two consecutive iterations is small, i.e. $\sum_{i=1}^{F} \| \Delta E_s^{(k)}(\omega_i) - \Delta E_s^{(k-1)}(\omega_i) \|_{L^2}^2 < \kappa$, with $\kappa > 0$ a small number, and F being the number of frequencies employed, then the thresholding operation is applied (see Fig. 3).

Conversely from the standard ISTA, the proposed approach relies on a set of thresholds which goes from a maximum down to a minimum value for each DBIM iteration. Thus, the selection of the thresholding interval represents an important

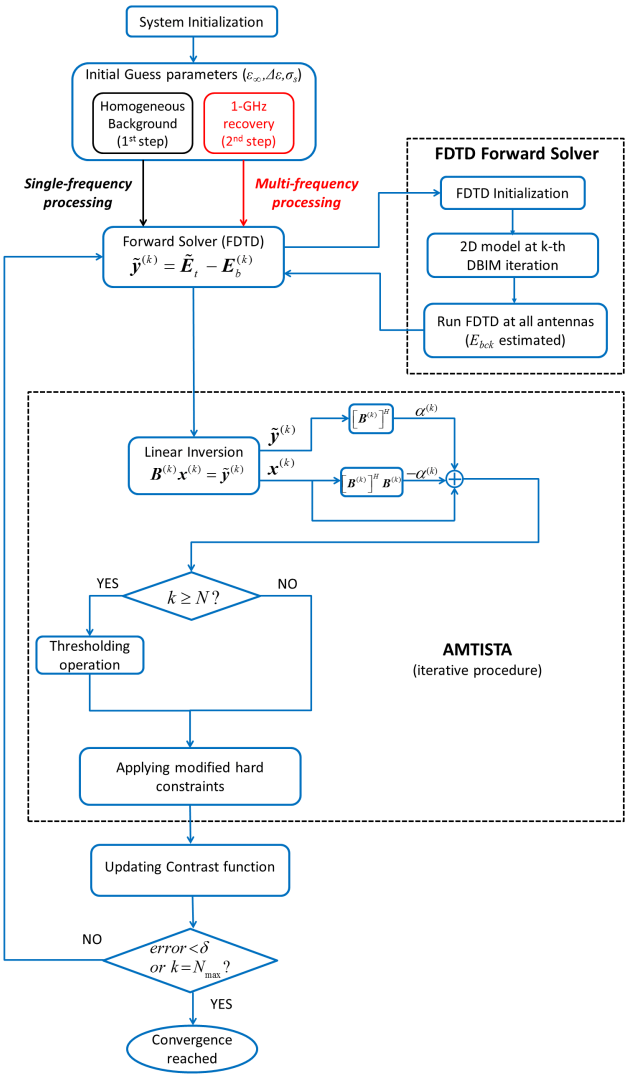

Fig. 3. Flow chart for the proposed AMTISTA approach. N is the number of iterations after which the adaptive criterion for the regularization parameter is applied, N_{max} is the maximum number of iterations selected for the DBIM procedure and δ is a small number employed as threshold for the stopping criterion on the residual error.

task. For each DBIM iteration, the AMTISTA threshold is applied moving from the highest value to the lowest one in the selected range by using a small enough step-size.

The generic iteration of the AMTISTA approach can be described mathematically, for a fixed DBIM iteration, as:

$$\begin{aligned}\mathbf{x}_{(i+1)}^{(k)} = \mathcal{T}_{\left[\lambda_{(db),max}^{(k)}\cdot\alpha^{(k)},\lambda_{(db),min}^{(k)}\cdot\alpha^{(k)}\right]}\Big(\mathbf{x}_{(i)}^{(k)} + \\ +\alpha^{(k)}\left[\mathbf{B}^{(k)}\right]^{\dagger}\left(\tilde{\mathbf{y}}^{(k)} - \mathbf{B}^{(k)}\mathbf{x}_{(i)}^{(k)}\right)\Big), \\ i = 1, \cdots, N_{ISTA},\end{aligned} \tag{8}$$

in which the thresholds have been selected by means of an

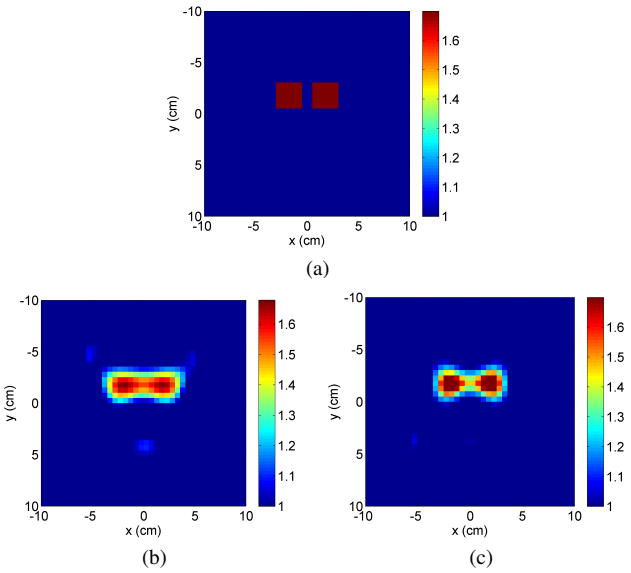

Fig. 4. Testing resolution capabilities of the proposed imaging algorithm. (a) Reference permettivity profile and retrieved functions by using (b) standard CGLS and (c) the proposed AMTISTA approach.

TABLE I
DEBYE PARAMETERS OF THE BREAST TISSUES IN THE FREQUENCY RANGE 0.5-3.5 GHZ

Material (mean value)	ϵ_∞	$\Delta\epsilon$	σ_s
Adipose tissue	4.68	3.21	0.0881
Fibroglandular tissue	17.3	19.4	0.535
Dry skin	18.4	21.9	0.737

automatic and adaptive criterion:

$$\begin{aligned}
\lambda^{(k)}_{(db),max} &= \beta_{max} \cdot \xi^{(k-1)}_{db}\,, \\
\lambda^{(k)}_{(db),min} &= \beta_{min} \cdot \xi^{(k-1)}_{db}\,, \\
\xi^{(k)}_{db} &= \left\langle \left| \mathbf{db}^{(k)} \right| \right\rangle = \frac{1}{N_{ID}} \sum_{i=1}^{N_{ID}} \left| \mathbf{db}^{(k)}\,(i) \right|\,, \\
\mathbf{db}^{(k)} &= \left\{ \boldsymbol{\epsilon}^{(k)}_\infty, \Delta\boldsymbol{\epsilon}^{(k)}, \boldsymbol{\sigma}^{(k)}_s \right\}\,,
\end{aligned} \tag{9}$$

in which the convergence parameter $\alpha^{(k)}$ is the same used in Section II for the ISTA approach, and the mathematical notation "$\langle \cdot \rangle$" refers to an averaging operation on all the pixels inside the breast, which is equal to N_{ID}, and $|\cdot|$ refers to the absolute value operator. Regarding the optimal selection of the β parameters, a numerical qualitative validation of the proposed empirical choice is reported and discussed in Section IV.

The proposed setup for the thresholding parameters allows an automatic and adaptive selection of the values to be employed, exploiting the knowledge of the previous step recovery to choose the optimal parameters for the selective thresholding. Such a choice drives into better reconstruction performance compared to standard inversion strategies. This criterion has been tested in different numerical scenarios, exhibiting general validity and providing an interesting unsupervised approach.

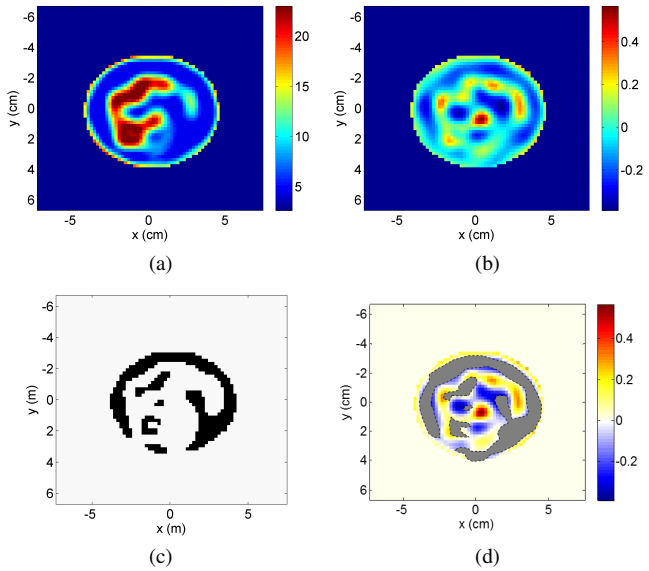

Fig. 5. Example of application of the modified hard constraints on a breast phantom (ID: 070604PA1). (a) $\boldsymbol{\epsilon}_\infty$ at the k-th DBIM iteration; (b) updating contrast function related to $\boldsymbol{\epsilon}_\infty$; (c) saturated pixels (black ones refer to the saturated pixels to be windowed); (d) new "masked" updating contrast function (the grey areas represent the saturated areas which are not updated and processed any more in the DBIM).

C. Performance

We first demonstrate the enhanced resolution of the DBIM-AMTISTA algorithm by considering the reconstruction of two rectangular scatterers in a homogeneous background. Figure 4 shows a numerical example with two non-weak scatterers of size $\lambda_b/2$ located at a distance of $\lambda_b/10$ from each other. It is easy to observe that using the AMTISTA approach as the solver at each DBIM iteration resolves the targets more clearly than a standard conjugate gradient least square (CGLS) linear solver, suggesting that thresholding methods can improve resolution relative to conventional L^2-based linear solver.

An example of the value of incorporating bounds on Debye parameters as constraints inside the AMTISTA solver is illustrated in Fig. 5. This figure shows an example of the values for the estimated unknown coefficients $\boldsymbol{\varrho}^{(k)}$ and of the complex permittivity parameters $\boldsymbol{\epsilon}^{(k)}$ at the k-th iteration of the minimization procedure. At this iteration, most pixels in the updating contrast function correspond to saturated pixels which will be not processed in the following DBIM iterations. The same principle has been applied for all the Debye unknowns, which allowed to reduce further the normalised residual error in the functional trend, i.e. an improvement in the quality of the recovery.

IV. NUMERICAL RESULTS

A. Reconstructions from numerical two-dimensional breast phantom data

As in our previous work with thresholding methods [28], [32], we have evaluated the proposed algorithm using simulated data from realistic numerical breast phantoms taken from the university of Wisconsin Madison repository [59], [60].

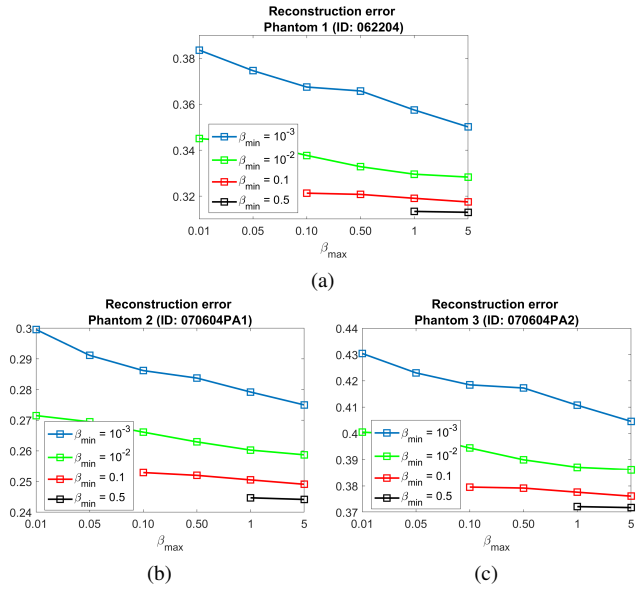

Fig. 6. Normalized reconstruction error for the choice of the optimal β parameters (SNR = 30 dB). The reconstruction error has been evaluated on the complex permittivity as $\frac{\|\epsilon_{\hat{x}}-\epsilon_{true}\|_2^2}{\|\epsilon_{true}\|_2^2}$, in which $\epsilon_{\hat{x}}$ is the retrieved complex profile and ϵ_{true} is the reference one. Different combinations of β_{max} and β_{min} were considered. Note that the plots in the figure do not have any value where $\beta_{max} < \beta_{min}$. (a) Breast phantom 062204, (b) breast phantom 070604PA1, (c) breast phantom 070604PA2.

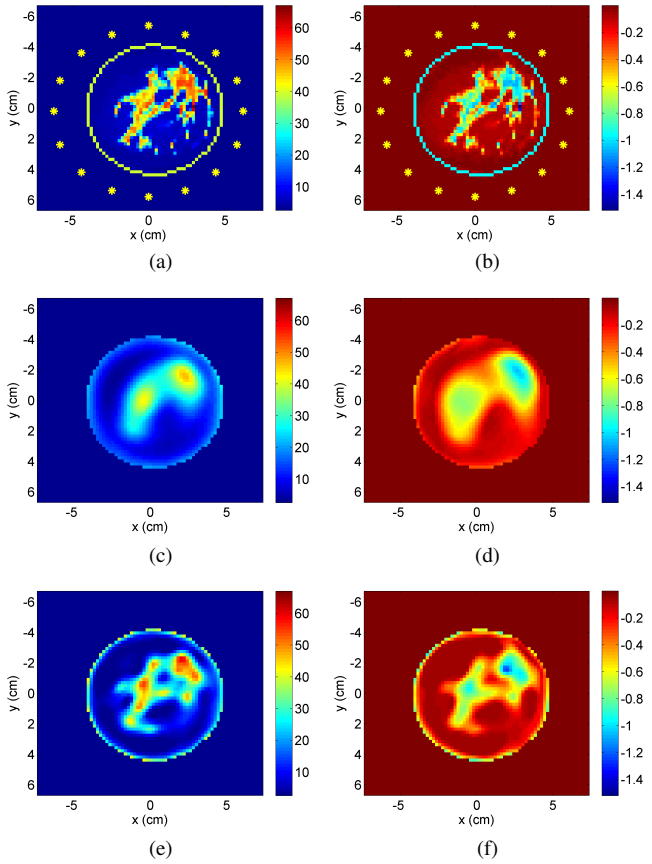

Fig. 7. Phantom 1 (ID: 062204, slice 106). (a)-(b): real and imaginary parts of the reference complex permittivity at 1 GHz; (c)-(d): recoveries by means of the adaptive ISTA approach [50] and (e)-(f) by employing AMTISTA. The yellow asterisks refer to antenna locations on the measurement circle.

We consider three different breast phantoms (ID = 062204 slice 106, ID = 070604PA1 slice 135, and ID = 070604PA2 slice 136), with percentage of fibroglandular tissue that varies between 25% and 75%. We assume that these phantoms are immersed in a lossless, non-dispersive matching medium whose Debye parameters are $\epsilon_\infty = 2.6, \Delta\epsilon = 0, \sigma_s = 0\,\mathrm{S/m}$. In all the following examples, data is acquired by sixteen filamentary antennas equally-spaced around the breast on a circle of radius equal to 6 cm, discarding the monostatic contributions and reciprocal data.

In the following, for the sake of space limitation and in order to make the discussion of the results more efficient, we show the real and imaginary parts of the complex permittivity function at a certain frequency instead of its Debye parameters.

The reconstruction performance and its accuracy have been estimated via two normalized root mean square errors defined as:

$$err_x\,(f) = \frac{\|\hat{x}\,(f) - x_{true}\,(f)\,\|_{L^2}^2}{\|x_{true}\,(f)\,\|_{L^2}^2}, \quad \text{with} \quad x = \{\epsilon', \epsilon''\}, \tag{10}$$

in which $\hat{\epsilon}'\,(f)$ and $\hat{\epsilon}''\,(f)$ are the estimated real and imaginary parts of the retrieved permittivity profile, while ϵ'_{true} and ϵ''_{true} represent the reference profiles.

The inversion process consists of two steps: the first step uses single-frequency data at 1 GHz, and its output is used as the initial guess in the second step, which involves a multi-frequency reconstruction. The advantages of this approach in reconstructing breast phantoms have been demonstrated in [29], [47]. We chose to use frequencies up to 2 GHz which represent a good trade-off between penetration depth and imaging resolution [61], [62]. This choice is also in agreement with the selected number of antennas based on the theoretical analysis of [63].

The choice of the proper frequency step-size does not represent a trivial task, and has not been studied in depth, to the best of authors' knowledge. Therefore, we have performed reconstructions for two of the phantoms using different frequency spacings. Respective reconstruction errors calculated by (10) are reported in Table II. It is easy to observe that a 200 MHz spacing seems to be the right choice, both for the phantoms with a high percentage of fibro-glandular tissues (ID: 070604PA1) as well as for mostly-adipose-tissue phantom (ID: 062204).

Regarding the choice of the β parameters, a numerical analysis has been performed and reported in Fig. 6. In order to select these parameters properly, different values for both β_{max} and β_{min} have been considered. It is easy to observe that the higher the value of β_{min} is, the less relevant the value of β_{max} is. This feature is quite interesting and allows a certain level of freedom in the choice of β_{max}. Thus in the following numerical simulations, we chose $\beta_{min} = 0.5$ and $\beta_{max} = 1$. This regularization strategy outperforms the standard processing, as shown in Fig. 7, 8 and 9 for a signal-to-noise ratio equal to 60 dB, driving into lower reconstruction errors and faster computation.

TABLE II
NORMALIZED MEAN SQUARE ERRORS FOR THE REAL AND IMAGINARY PARTS OF RELATIVE COMPLEX PERMITTIVITY AS FUNCTION OF DATA FREQUENCY SPACING.

	Phantom 1 (ID: 062204)			**Phantom 2 (ID: 070604PA1)**		
Frequency spacing	0.2 GHz	0.5 GHz	1 GHz	0.2 GHz	0.5 GHz	1 GHz
$\mathbf{err}_{\epsilon'}$	0.17	0.17	0.17	0.18	0.21	0.23
$\mathbf{err}_{\epsilon''}$	0.24	0.24	0.25	0.25	0.31	0.39

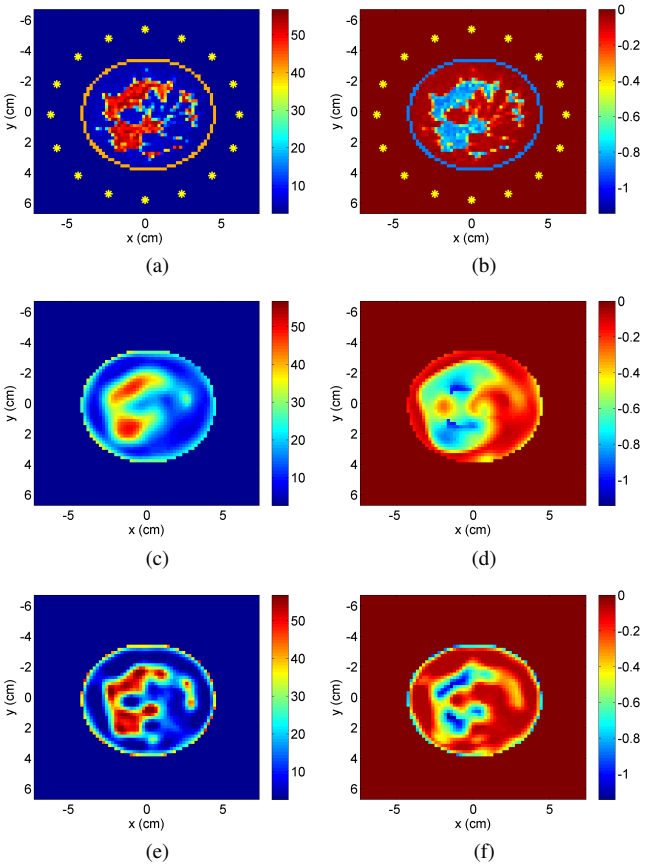

Fig. 8. Phantom 2 (ID: 070604PA1, slice 135). (a)-(b): real and imaginary parts of the reference complex permittivity at 1 GHz; (c)-(d): recoveries by means of the adaptive ISTA approach [50] and (e)-(f) by employing AMTISTA. The yellow asterisks refer to antenna locations on the measurement circle.

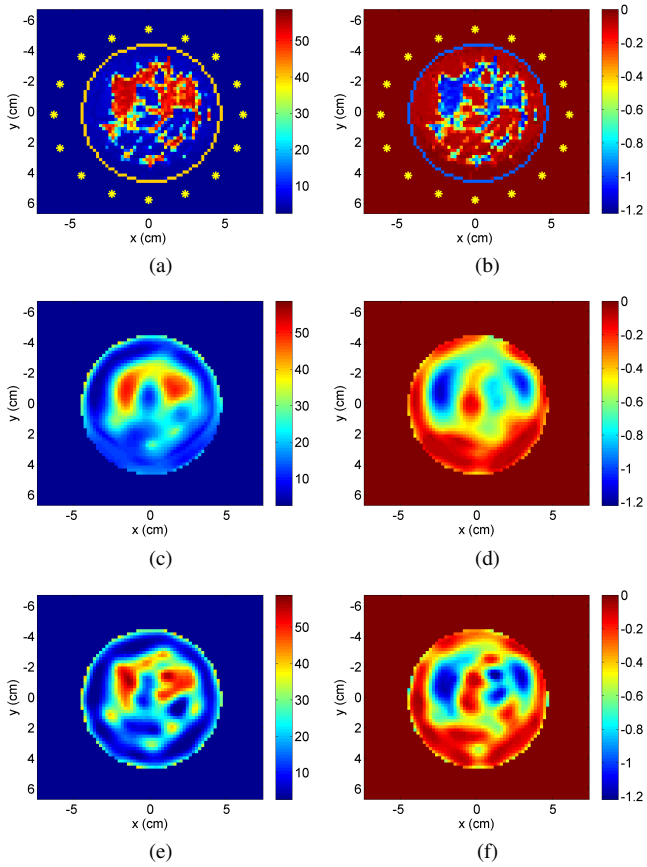

Fig. 9. Phantom 3 (ID: 070604PA2, slice 136). (a)-(b): real and imaginary parts of the reference complex permittivity at 1 GHz; (c)-(d): recoveries by means of the adaptive ISTA approach [50] and (e)-(f) by employing AMTISTA. The yellow asterisks refer to antenna locations on the measurement circle.

Fig. 10 shows the plot of the normalised residual errors for different breast phantoms along the second-step DBIM iterations. The proposed approach is tested and compared with other standard methods described previously in Section II-B. As shown in Fig. 10, it is easy to observe that the use of a fixed regularization parameter as suggested in [21] provides good recovery performance in case of high SNR values, while an adaptive regularization strategy, like the one suggested in [50], works well with different SNR values.

The respective errors are listed in Table III for different SNRs relative to the energy of the total field at all the employed frequencies. The amount of white Gaussian noise added in the numerical simulations has been evaluated starting from the power of the useful signal, i.e.:

$$P_y = \frac{1}{M \cdot n_f} \sum_{i=1}^{M} \sum_{j=1}^{n_f} y_{ij}^2 \,, \tag{11}$$

in which M is the number of multiview-multistatic data per each frequency, n_f is the number of frequencies employed in the inversion procedure and y_{ij} is the signal collected at the i-th transmitter-receiver couple and for the j-th frequency.

A quick comparison of the AMTISTA results in Fig. 7, 8 and 9 to those using the standard regularization parameters in the ISTA framework suggests an improved performance for the proposed approach (only the adpative regularization parameter case is reported in the previous images since it has the lowest reconstruction error compared to the fixed case). The accuracy of the retrieved profiles is quite good and could be improved

TABLE III
COMPARISON OF RECOVERY PERFORMANCE AS FUNCTION OF THE SNR VALUE FOR BOTH ADAPTIVE ISTA [50] AND THE PROPOSED AMTISTA APPROACH AT 1 GHZ FREQUENCY.

	ISTA						AMTISTA					
	$\mathbf{err}_{\epsilon'}$			$\mathbf{err}_{\epsilon'}$			$\mathbf{err}_{\epsilon'}$			$\mathbf{err}_{\epsilon'}$		
SNR	**60**	**30**	**20**	**60**	**30**	**20**	**60**	**30**	**20**	**60**	**30**	**20**
Phantom 1	0.55	0.55	0.56	0.88	0.89	0.91	0.21	0.21	0.22	0.60	0.60	0.62
Phantom 2	0.47	0.47	0.48	0.93	0.94	0.96	0.13	0.13	0.14	0.71	0.70	0.81
Phantom 3	0.37	0.38	0.39	0.85	0.87	0.90	0.25	0.27	0.29	0.64	0.65	0.69

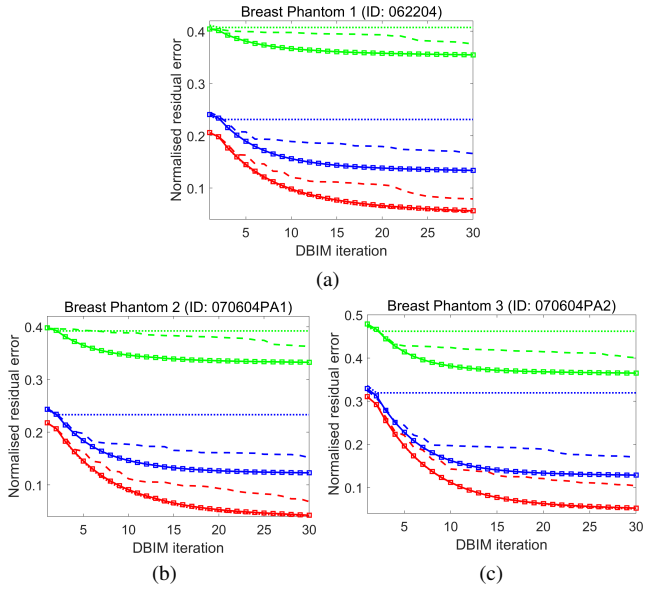

Fig. 10. Normalised residual errors plots for three breast phantoms. Three different values of the signal-to-noise ratio are considered: 60 dB (red lines), 30 dB (blue lines) and 20 dB (green lines). The proposed approach AMTISTA (continuous line with square markers) is compared with other standard regularization strategies (dashed lines for adaptive regularization [50] and dotted ones for fixed parameters [21]). (a) Breast phantom 062204, (b) breast phantom 070604PA1, (c) breast phantom 070604PA2.

further by exploiting a more suitable decomposition basis which is able to enforce sparsity in the signal representation. Moreover, the method is robust against noise as proved by the values proposed in Table III. It is worth to note that the proposed approach is blind and does not require any prior information, conversely from the standard ISTA approaches described in Section II-B.

B. Performance assessment using data from a three-dimensional CAD model

As our final aim is the use of this algorithm for microwave imaging in clinical applications, it is important to test its applicability to data from a more realistic system that could be used in microwave medical imaging experiments. To this end, we have considered a three-dimensional numerical model that employs a cylindrical imaging tank filled with a realistic coupling medium, fully modelled printed monopole antenna, and a simple target to be reconstructed. This represents an intermediate step before testing with experimental data [64]–[68], and can help us to isolate systematic model errors from random errors that may occur in experimental measurements.

An overview of our three-dimensional (3-D) case of study is reported in Fig. 11. The proposed setup consists of a

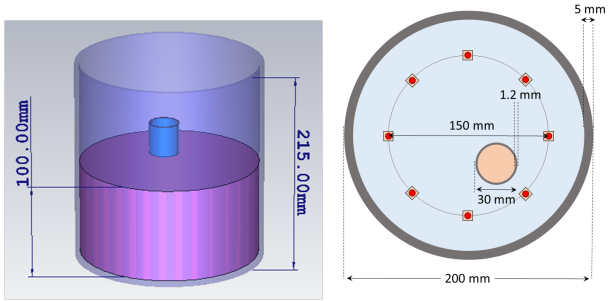

Fig. 11. Three-dimensional numerical testbed for the data generation: front view (a) and top view (b). The red symbols identify the antenna locations.

plastic cylindrical tank filled with triton as matching medium $\left(\epsilon_{\infty}^{trit} = 3.51, \Delta\epsilon^{trit} = 2.58, \sigma_s^{trit} = 0.06\,\text{S/m}\right)$. The target is a plastic cylinder filled with water that is assumed to be non-dispersive $\left(\epsilon_{\infty}^{wat} = 78, \Delta\epsilon^{wat} = 0, \sigma_s^{wat} = 1.56\,\text{S/m}\right)$. Eight printed monopoles have been used as both transmitting as well as receiving antennas in order to realize a multistatic system (Fig. 11-b). The system has been simulated using the commercial electromagnetic software CST Microwave Studio solver.

As this imaging problem does not require high resolution, we have performed single-frequency reconstructions assuming knowledge of the background medium properties as our initial guess. To reduce the ill-posedness of the electromagnetic inverse scattering problem at hand, a spatial projection operator has been employed in order to reduce the cardinality of the geometry, i.e. to reduce the number of unknowns. In this example, the initial fine grid of the imaging domain is projected on a coarser grid in the inversion procedure, moving from 7200 to 1800 unknowns approximately.

Prior to inversion, we applied a "standard empty-tank" calibration procedure [69]. Two different three-dimensional (3-D) CST Microwave Studio simulations were run using this software in order to obtain the incident field at the receiver locations $\left(E_{inc}^{CST,3D}\right)$, i.e. the field without the target, and the total field $\left(E_{tot}^{CST,3D}\right)$, i.e. the field with the target inside the tank. Another two-dimensional simulation was run to evaluate the incident field at receiver locations via in-house FDTD codes $\left(E_{inc}^{FDTD,2D}\right)$. Then, the new "calibrated" data per each

frequency at receiver locations was calculated by:

$$E_{cal}\left(f\right)=\frac{E_{inc}^{FDTD,2D}\left(f\right)}{E_{inc}^{CST,3D}\left(f\right)}\cdot E_{tot}^{CST,3D}\left(f\right). \qquad (12)$$

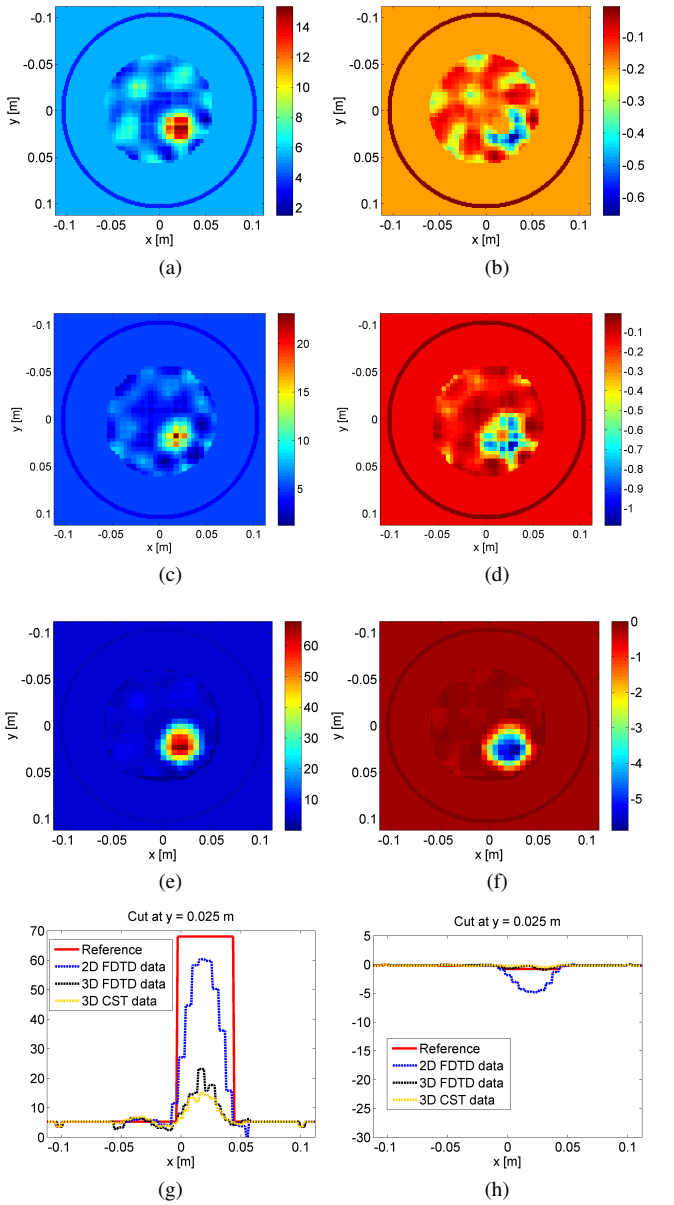

Fig. 12. Recovery at 2 GHz with triton as matching medium. Real and imaginary parts of retrieved complex relative permittivities for: realistic antennas (3-D CST data) (a)-(b), ideal dipole antennas (3-D FDTD data) (c)-(d) and 2-D ideal sources (2-D FDTD data). A cut at y = 2.5 cm is plotted for both real and imaginary parts in (g) and (h).

The reason for calling (12) a "calibrated" field is that it is the result of a numerical calibration procedure to scale the CST results to the FDTD results, similar to standard calibration of experimental data (e.g., [69]). This can be seen as an attempt to convert the collected numerical data to the assumed numerical model using a so-called "incident field" calibration.

Reconstructions at 2 GHz are shown in Fig. 12. The target can be clearly detected, but its complex permittivity values are underestimated. This is not unexpected given that we considered a 2-D forward solver with filamentary antennas in our imaging algorithm to invert 3-D data.

Fig. 12 tries to provide an overview of the limitations related to a 2-D processing for the inversion procedure starting from 3-D data in a step-wise fashion. It starts with the processing of 3-D CST data which takes into account the use of realistic monopole antennas immersed in a triton solution to image a water circular target.

As a matter of fact, the main difference between our 2-D in-house FDTD model and the CST one shown in Fig. 11 is related to use of realistic antennas which are not properly taken into account in the inversion procedure, introducing propagation and scattering errors. Furthermore, the 3-D nature of the problem affects the 2-D inversion, introducing modelling errors which are also related to the multi-scattering phenomena arising from the different layers, e.g. the bottom of the tank and the top interface between matching medium and air. Fig. 12(a)-(b) shows the impact of these modelling errors on the retrieved profiles.

With the aim of isolating the effect of antenna modelling and to study only the limitations introduced by the 3-D geometry processed by 2-D codes, we used the same scenario but with ideal dipole antennas. Fig. 12(c)-(d) shows some recoveries obtained by means of processing 3-D FDTD in-house data in which ideal dipole antennas have been employed. Compared to Fig. 12(a)-(b), the recoveries are improved and the permittivity values of the retrieved target are closer to the true ones.

Finally, Fig. 12(e)-(f) shows the retrieved profiles by processing 2-D FDTD data of the corresponding 3-D model of Fig. 11. An overview of all the recoveries with a focus on the cut at $y = 2.5$ cm is reported in Fig. 12(g)-(h), illustrating the limitations and advantages of the proposed approach.

In order to explore and quantify the importance of modelling properly the employed realistic antennas and the impact of the multi-scattering interactions related to the 3-D geometry, Fig. 13 considers the ratio between the calibrated field E_{cal}, i.e. the 3-D CST field multiplied by the calibration coefficients, and the 2-D FDTD field evaluated with the same geometry but by using in-house codes based on ideal sources $E_{tot}^{FDTD,2D}$.

To perform this analysis, a quantitative relative error was evaluated as:

$$err_{rel}\left(f\right)=\frac{\|E_{cal}\left(f\right)-E_{tot}^{FDTD,2D}\left(f\right)\|_{L^2}^2}{\|E_{tot}^{FDTD,2D}\left(f\right)\|_{L^2}^2}. \qquad (13)$$

Two main frequencies have been considered and reported in the text, i.e. $f = 1.2$ GHz and $f = 2$ GHz, whose relative errors are shown in Fig. 13. From the analysis of this figure, it is easy to observe that the errors at 1.2 GHz are higher than those ones at 2.0 GHz, and the motivation is related to the design of the considered antenna, which operates better at 2 GHz rather than at 1.2 GHz [66]. Furthermore, it is evident that there are higher differences in the values of the electric fields for all those antennas that are farther from the monostatic contribution.

For the sake of clarity, it is worth to mention that in standard MWI the targets to be retrieved are usually characterised by low values of the contrast function $\chi = \frac{\epsilon_{targ}-\epsilon_b}{\epsilon_b}$, in which ϵ_{targ} is the complex permittivity function of the considered

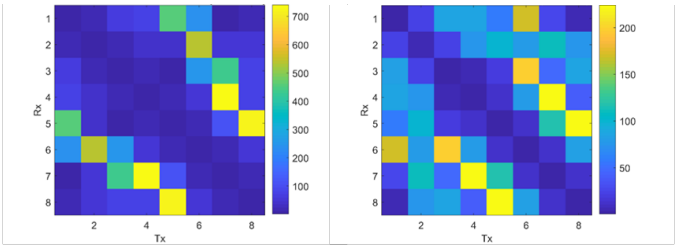

(a) (b)

Fig. 13. Relative errors between calibrated 3-D CST data and simulated 2-D FDTD data with ideal antennas for different frequencies: (a) 1.2 GHz and (b) 2 GHz.

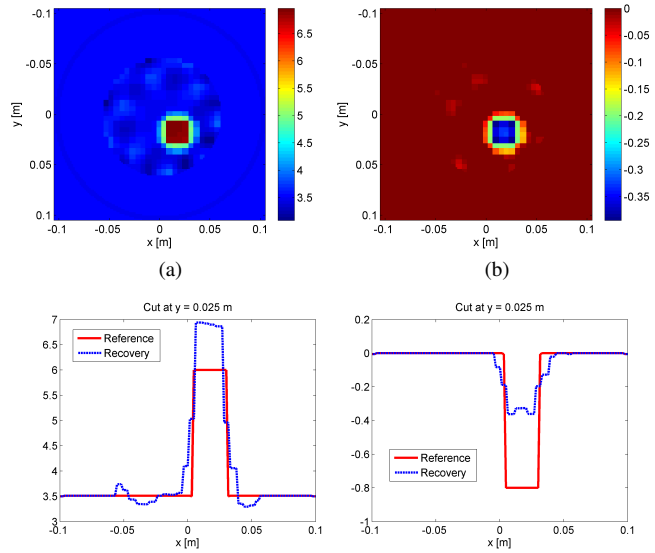

(a) (b)

(c) (d)

Fig. 14. Same as Fig. 12(c)-(d), but with a lower contrast target $\left(\epsilon_\infty^{targ} = 6, \Delta\epsilon^{targ} = 0, \sigma_s^{targ} = 0.1\,\text{S/m}\right)$. Real (a) and imaginary (b) parts of complex relative permittivity. Plots of real (c) and imaginary (d) parts of recovered (blue, dashed lines) and reference (red, continuous lines) profiles.

scatterers and ϵ_b is complex permittivity of the background. Typical values of the contrast function are lower than one, and this assumption allows to limit the non-linear scattering phenomena in order to reach the convergence and obtain good recovery performance, but in the example proposed in this section, the value of the contrast function χ is quite high (more than twenty), and this dramatically limits the quality of the recovery.

Therefore, to conclude the analysis, we added one last example to test the 2-D inversion performance of the proposed approach starting from the processing of 3-D data with a much lower contrast profile $(\epsilon_\infty^{targ} = 6, \Delta\epsilon^{targ} = 0, \sigma_s^{targ} = 0.1\,\text{S/m})$. The results of inversion procedure are reported in Fig. 14, with a focus on the cut at $y = 2.5$ cm. It is easy to observe that the use of lower contrast profiles allows to improve the recovery performance from 3-D data, but still suffers (as well-known) for the 2-D modelling of the inversion strategy.

Nevertheless the limitations related to the use a of 2-D model to process 3-D data with realistic antennas, the quality of recoveries can be improved considerably by exploiting a scattered-field calibration method [69], which results in more accurate reconstructions compared to the incident-field one at the price of a higher experimental complexity.

V. Conclusion

In this paper a novel adaptive shrinkage-thresholding method for quantitative medical imaging applications of breast tissues has been presented. Important novelties of this approach are the use of multiple thresholds to recover the different unknowns in the Debye model as well as the adaptive selection of these thresholds.

Moreover, we have shown that employing modified hard constraints inside the linear step of the inversion procedure can enhance reconstruction quality.

The performance of the method has been tested in complex non-sparse scenarios for breast imaging purposes, showing a good agreement with the reference profiles for three different anthropomorphic breast phantoms with different percentage of fibroglandular/adipose tissues. Performed reconstructions have been compared with the standard sparse-based approach named ISTA, obtaining better recoveries and more stable results. Moreover, some preliminary three-dimensional numerical simulations to test the proposed inversion scheme have been considered.

Beyond moving to more realistic cases, our future work will focus on the choice of a proper decomposition basis which can enforce the sparsity of the problem while trying to reduce the ill-posedness of the inverse problem.

Acknowledgment

This work was supported in part by COST Action TD1301, MiMed, through a short term scientific mission of the first author to MediWiSe — Medical Wireless Sensing Ltd, 42 New Road, London E1 2AX, UK.

We thank Ziwen Guo from King's College London UK for providing the 3-D data processed in the paper.

References

[1] M. Ambrosanio, R. Scapaticci, and L. Crocco, "A simple quantitative inversion approach for microwave imaging in embedded systems," *International Journal of Antennas and Propagation*, vol. 501, pp. 129823, 2015.

[2] R. Scapaticci, L. Di Donato, I. Catapano, and L. Crocco, "A feasibility study on microwave imaging for brain stroke monitoring," *Progress In Electromagnetics Research B*, vol. 40, pp. 305–324, 2012.

[3] M. Ostadrahimi, P. Mojabi, A. Zakaria, J. LoVetri, and L. Shafai, "Enhancement of Gauss–Newton inversion method for biological tissue imaging," *IEEE Transactions on Microwave Theory and Techniques*, vol. 61, no. 9, pp. 3424–3434, 2013.

[4] E. J. Bond, X. Li, S. C. Hagness, and B. D. Van Veen, "Microwave imaging via space-time beamforming for early detection of breast cancer," *IEEE Transactions on Antennas and Propagation*, vol. 51, no. 8, pp. 1690–1705, 2003.

[5] O. M. Bucci, L. Crocco, and R. Scapaticci, "On the optimal measurement configuration for magnetic nanoparticles-enhanced breast cancer microwave imaging," *IEEE Transactions on Biomedical Engineering*, vol. 62, no. 2, pp. 407–414, 2015.

[6] P. Kosmas and C. M. Rappaport, "A matched-filter FDTD-based time reversal approach for microwave breast cancer detection," *IEEE Transactions on Antennas and Propagation*, vol. 54, no. 4, pp. 1257–1264, 2006.

[7] P. Kosmas and C.M. Rappaport, "FDTD-based time reversal for microwave breast cancer detection-localization in three dimensions," *IEEE Transactions on Microwave Theory and Techniques*, vol. 54, no. 4, pp. 1921–1927, 2006.

[8] T. M. Grzegorczyk, P. M. Meaney, and K. D. Paulsen, "Microwave tomographic imaging for breast cancer chemotherapy monitoring," in *The 8th European Conference on Antennas and Propagation (EuCAP 2014)*. IEEE, 2014, pp. 702–703.

[9] A. Baran, D. Kurrant, E. Fear, and J. Lo Vetri, "Monitoring breast cancer treatment progress with microwave tomography and radar-based tissue-regions estimation," in *2015 9th European Conference on Antennas and Propagation (EuCAP)*. IEEE, 2015, pp. 1–2.

[10] T. M. Grzegorczyk, P. M. Meaney, P. A. Kaufman, K. D. Paulsen, et al., "Fast 3-D tomographic microwave imaging for breast cancer detection," *IEEE Transactions on Medical Imaging*, vol. 31, no. 8, pp. 1584–1592, 2012.

[11] L. M. Neira, B. D. Van Veen, and S. C. Hagness, "Investigation of high-resolution microwave breast imaging using a 3-D inverse scattering algorithm with a variable-strength spatial prior constraint," in *Radio Science Meeting (Joint with AP-S Symposium), 2015 USNC-URSI*. IEEE, 2015, pp. 302–302.

[12] M. Ambrosanio, P. Kosmas, and V. Pascazio, "An adaptive multi-threshold iterative shrinkage algorithm for microwave imaging applications," in *2016 10th European Conference on Antennas and Propagation (EuCAP)*. IEEE, 2016, pp. 1–3.

[13] T. J. Cui, W. C. Chew, A. A. Aydiner, and S. Chen, "Inverse scattering of two-dimensional dielectric objects buried in a lossy earth using the distorted Born iterative method," *IEEE Transactions on Geoscience and Remote Sensing*, vol. 39, no. 2, pp. 339–346, 2001.

[14] D. W. Winters, D. J. Shea, P. Kosmas, D. B. Van Veen, and S. C. Hagness, "Three-dimensional microwave breast imaging: dispersive dielectric properties estimation using patient-specific basis functions," *IEEE Transactions on Medical Imaging*, vol. 28, no. 7, pp. 969–981, July 2009.

[15] W. C. Chew and Y. M. Wang, "Reconstruction of two-dimensional permittivity distribution using the distorted Born iterative method," *IEEE transactions on medical imaging*, vol. 9, no. 2, pp. 218–225, 1990.

[16] D. L. Donoho, "Compressive sensing," *IEEE Transactions on Information Theory*, vol. 52, pp. 1289–1306, 2006.

[17] W. Dai and O. Milenkovic, "Subspace pursuit for compressive sensing signal reconstruction," *IEEE Transactions on Information Theory*, vol. 55, no. 5, pp. 2230–2249, 2009.

[18] E. Candes and M.B. Wakin, "An Introduction to Compressive Sampling," *IEEE Signal Processing Magazine*, vol. 25, pp. 21–30, March 2008.

[19] S Foucart and H. Rauhut, *A Mathematical Introduction to Compressive Sensing*, Applied and Numerical Harmonic Analysis. Springer Science, 2013.

[20] C. Estatico, M. Pastorino, and A. Randazzo, "A novel microwave imaging approach based on regularization in Banach spaces," *IEEE Transactions on Antennas and Propagation*, vol. 60, no. 7, pp. 3373–3381, 2012.

[21] S. S. Chen, D. L. Donoho, and M. A. Saunders, "Atomic decomposition by basis pursuit," *SIAM review*, vol. 43, no. 1, pp. 129–159, 2001.

[22] R. Tibshirani, "Regression shrinkage and selection via the LASSO," *Journal of the Royal Statistical Society. Series B (Methodological)*, pp. 267–288, 1996.

[23] L. Di Donato, M. Bevacqua, L. Crocco, and T. Isernia, "Exploiting compressive sensing in microwave tomography and inverse scattering," in *The 8th European Conference on Antennas and Propagation (EuCAP 2014)*. IEEE, 2014, pp. 1247–1249.

[24] J. A. Tropp, A. C. Gilbert, and M. J. Strauss, "Algorithms for simultaneous sparse approximation. Part I: Greedy pursuit," *Signal Processing*, vol. 86, no. 3, pp. 572–588, 2006.

[25] L. Poli, G. Oliveri, F. Viani, and A. Massa, "MT–BCS-based microwave imaging approach through minimum-norm current expansion," *IEEE Transactions on Antennas and Propagation*, vol. 61, no. 9, pp. 4722–4732, 2013.

[26] A. Massa, P. Rocca, and G. Oliveri, "Compressive sensing in electromagnetics-a review," *IEEE Antennas and Propagation Magazine*, vol. 57, no. 1, pp. 224–238, 2015.

[27] V. Pascazio and G. Ferraiuolo, "Statistical regularization in linearized microwave imaging through MRF-based MAP estimation: hyperparameter estimation and image computation," *IEEE transactions on image processing*, vol. 12, no. 5, pp. 572–582, 2003.

[28] M. Azghani, P. Kosmas, and F. Marvasti, "Microwave medical imaging based on sparsity and an iterative method with adaptive thresholding," *IEEE Transactions on Medical Imaging*, vol. 34, no. 2, pp. 357–365, Feb. 2015.

[29] Z. Miao and P. Kosmas, "Multiple-frequency DBIM-TwIST algorithm for microwave breast imaging," *IEEE Trans. Antennas Propag.*, vol. 65, no. 5, pp. 2507–2516, 2017.

[30] A. Beck and M. Teboulle, "A fast iterative shrinkage-thresholding algorithm for linear inverse problems," *Journal of Imaging Sciences*, vol. 2, no. 1, pp. 183–202, 2009.

[31] M. Fornasier and H. Rauhut, "Compressive sensing," in *Handbook of mathematical methods in imaging*, pp. 187–228. Springer, 2011.

[32] Z. Miao and P. Kosmas, "Microwave breast imaging based on an optimized two-step iterative shrinkage/thresholding method," in *2015 9th European Conference on Antennas and Propagation (EuCAP)*. IEEE, 2015, pp. 1–4.

[33] M. Bevacqua and R. Scapaticci, "Magnetic nanoparticles enhanced breast cancer microwave imaging via compressive sensing," in *2015 9th European Conference on Antennas and Propagation (EuCAP)*. IEEE, 2015, pp. 1–4.

[34] G. Leone, R. Persico, and R. Pierri, "Inverse scattering under the distorted Born approximation for cylindrical geometries," *JOSA A*, vol. 16, no. 7, pp. 1779–1787, 1999.

[35] M. Slaney, A. C. Kak, and L. E. Larsen, "Limitations of imaging with first-order diffraction tomography," *IEEE Transactions on Microwave Theory and Techniques*, vol. 32, no. 8, pp. 860–874, 1984.

[36] J.E. Gubernatis, E. Domany, J.A. Krumhansl, and M. Huberman, "The Born approximation in the theory of the scattering of elastic waves by flaws," *Journal of Applied Physics*, vol. 48, no. 7, pp. 2812–2819, 1977.

[37] J.A. Hudson and J.R. Heritage, "The use of the Born approximation in seismic scattering problems," *Geophysical Journal International*, vol. 66, no. 1, pp. 221–240, 1981.

[38] L. Poli, G. Oliveri, and A. Massa, "Microwave imaging within the first-order Born approximation by means of the contrast-field bayesian compressive sensing," *IEEE Transactions on Antennas and Propagation*, vol. 60, no. 6, pp. 2865–2879, 2012.

[39] D. Colton and R. Krees, *Inverse Acoustic and Electromagnetic Scattering Theory*, Springer-Verlag, Berlin, Germany, 1992.

[40] M. Bertero and P. Boccacci, *Introduction to Inverse Problems in Imaging*, Institute of Physics Publishing, Bristol, U.K., 1998.

[41] L., T. Isernia, V. Pascazio, and R. Pierri, "A Nonlinear Estimation Method in Tomographic Imaging," *IEEE Transactions on Geoscience and Remote Sensing*, vol. 35, pp. 910–923, July 1997.

[42] J. Richmond, "Scattering by a dielectric cylinder of arbitrary cross section shape," *IEEE Transactions on Antennas and Propagation*, vol. 13, pp. 334–341, 1965.

[43] P.M. Meaney, M.W. Fanning, T. Raynolds, C.J. Fox, Q.Q. Fang, C.A. Kogel, S.P. Poplack, and K.D. Paulsen, "Initial clinical experience with microwave breast imaging in women with normal mammography,," *Acad. Radiol.*, vol. 14, no. 2, pp. 207–218, February 2007.

[44] M. Lazebnik, L. McCartney, D. Popovic, C. B. Watkins, M. J. Lindstrom, J. Harter, S. Sewall, A. Magliocco, J. H. Booske, M. Okoniewski, et al., "A large-scale study of the ultrawideband microwave dielectric properties of normal breast tissue obtained from reduction surgeries," *Physics in medicine and biology*, vol. 52, no. 10, pp. 2637, 2007.

[45] S. Gabriel, R.W. Lau, and C. Gabriel, "The dielectric properties of biological tissues: III. parametric models for the dielectric spectrum of tissues," *Physics in medicine and biology*, vol. 41, no. 11, pp. 2271, 1996.

[46] O. M. Bucci, L. Crocco, T. Isernia, and V. Pascazio, "Inverse scattering problems with multi-frequency data: reconstruction capabilities and solution strategies," *IEEE Transactions on Geoscience and Remote Sensing*, vol. 38, pp. 1749–1756, July 2000.

[47] R. Scapaticci, P. Kosmas, and L. Crocco, "Wavelet based regularization for robust microwave imaging in medical applications," *IEEE Transactions on Biomedical Engineering*, vol. 62, no. 4, pp. 1195–1202, April 2015.

[48] L. Liang and Y. Xu, "Adaptive Landweber method to deblur images," *IEEE signal processing letters*, vol. 10, no. 5, pp. 129–132, 2003.

[49] D. L. Donoho, "De-noising by soft-thresholding," *IEEE transactions on information theory*, vol. 41, no. 3, pp. 613–627, 1995.

[50] J. Fang, Z. Xu, B. Zhang, W. Hong, and Y. Wu, "Fast compressed sensing SAR imaging based on approximated observation," *IEEE Journal of Selected Topics in Applied Earth Observations and Remote Sensing*, vol. 7, no. 1, pp. 352–363, 2014.

[51] A. Chambolle, R. A. De Vore, N. Y. Lee, and B. J. Lucier, "Nonlinear wavelet image processing: variational problems, compression, and noise removal through wavelet shrinkage," *IEEE Transactions on Image Processing*, vol. 7, no. 3, pp. 319–335, 1998.

[52] I. Daubechies, M. Defrise, and C. De Mol, "An iterative thresholding algorithm for linear inverse problems with a sparsity constraint," *Communications on pure and applied mathematics*, vol. 57, no. 11, pp. 1413–1457, 2004.
[53] J. Bioucas-Dias and M. Figueiredo, "A new TwIST: two-step iterative shrinkage/thresholding algorithms for image restoration," *IEEE Transactions on Image Processing*, vol. 16, no. 12, pp. 2992–3004, 2007.
[54] F. Bai, W. Philips, and A. Pizurica, "Quantitative microwave imaging based on a huber regularization," in *IEICE Information and Communication Technology Forum (ICTF-2013)*, 2013.
[55] P. Mojabi and J. Lo Vetri, "Enhancement of the Krylov subspace regularization for microwave biomedical imaging," *IEEE transactions on medical imaging*, vol. 28, no. 12, pp. 2015–2019, 2009.
[56] P. Lobel, C. Pichot, L. Blanc-Féraud, and M. Barlaud, "Microwave imaging: reconstructions from experimental data using conjugate gradient and enhancement by edge-preserving regularization," *International Journal of Imaging Systems and Technology*, vol. 8, no. 4, pp. 337–342, 1997.
[57] J. A. Roden and S. D. Gedney, "Convolutional PML (CPML): An efficient FDTD implementation of the CFS-PML for arbitrary media," *Microwave and optical technology letters*, vol. 27, no. 5, pp. 334–338, 2000.
[58] B. Eicke, "Iteration methods for convexly constrained ill-posed problems in Hilbert space," *Numerical Functional Analysis and Optimization*, vol. 13, no. 5-6, pp. 413–429, 1992.
[59] E. Zastrow, S. K. Davis, M. Lazebnik, F. Kelcz, B. D. Van Veen, and S. C. Hagness, "Database of 3D Grid-Based Numerical Breast Phantom for Use in Computational Electromagnetics Simulations," *IEEE Transactions on Biomedical Engineering*, vol. 55, no. 12, pp. 2792–2800, 2008.
[60] University of Wisconsin Cross-Disciplinary Electromagnetics Laboratory, "Breast phantom repository," https://uwcem.ece.wisc.edu/phantomRepository.html.
[61] I. Catapano, L. Di Donato, L. Crocco, O. M. Bucci, A. F. Morabito, T. Isernia, and R. Massa, "On quantitative microwave tomography of female breast," *Progress In Electromagnetics Research*, vol. 97, pp. 75–93, 2009.
[62] I. Catapano, L. Crocco, L. Di Donato, G. Angiulli, T. Isernia, A. Morabito, S. Tringali, and O.M. Bucci, "Guidelines for effective microwave breast imaging: a numerical assessment against 3D anthropomorphic phantoms," in *Antennas and Propagation (EuCAP), 2010 Proceedings of the Fourth European Conference on*. IEEE, 2010, pp. 1–5.
[63] O.M. Bucci and G. Franceschetti, "On the spatial bandwidth of scattered fields," *IEEE Transactions on Antennas and Propagation*, 1987.
[64] Mario R Casu, Marco Vacca, Jorge A Tobon, Azzurra Pulimeno, Imran Sarwar, Raffaele Solimene, and Francesca Vipiana, "A cots-based microwave imaging system for breast-cancer detection," *IEEE Transactions on Biomedical Circuits and Systems*, vol. 11, no. 4, pp. 804–814, 2017.
[65] P.M Meaney, M.W. Fanning, S.P. Dun Li, K.D. Poplack, and Paulsen, "A clinical prototype for active microwave imaging of the breast," *IEEE Transactions on Microwave Theory and Techniques*, vol. 48, no. 11, pp. 1841–1853, 2000.
[66] Maria Koutsoupidou, Panagiotis Kosmas, Syed Ahsan, Zhenzhuang Miao, Ioannis Sotiriou, and Themos Kallos, "Towards a microwave imaging prototype based on the DBIM-TwIST algorithm and a custom-made transceiver system," in *Electromagnetics in Advanced Applications (ICEAA), 2017 International Conference on*. IEEE, 2017, pp. 1004–1007.
[67] M Klemm, JA Leendertz, D Gibbins, IJ Craddock, A Preece, and R Benjamin, "Microwave radar-based breast cancer detection: Imaging in inhomogeneous breast phantoms," *IEEE Antennas and Wireless Propagation Letters*, vol. 8, pp. 1349–1352, 2009.
[68] Mohammad Asefi, Majid OstadRahimi, Amer Zakaria, and Joe LoVetri, "A 3-D dual-polarized near-field microwave imaging system," *IEEE Transactions on Microwave Theory and Techniques*, vol. 62, no. 8, pp. 1790–1797, 2014.
[69] M. Ostadrahimi, P. Mojabi, C. Gilmore, A. Zakaria, S. Noghanian, S. Pistorius, and J. Lo Vetri, "Analysis of incident field modeling and incident/scattered field calibration techniques in microwave tomography," *IEEE Antennas and Wireless Propagation Letters*, vol. 10, pp. 900–903, 2011.

Michele Ambrosanio (S'13-M'16) was born in Naples, Italy, in 1987. He received both B.S. and M.S. degrees (summa cum laude) in Biomedical Engineering from the University of Naples "Federico II" in 2009 and 2012, respectively, and his Ph.D. in Information Engineering in 2016 from the University of Naples "Parthenope", Italy. He was a visiting Ph.D. student at School of Natural and Mathematical Sciences, King's college, London from April to July 2015, and was at Mediwise L.t.d. from July to November 2015, working on biomedical applications of microwave imaging for diagnostic purposes in the framework of his Ph.D. program.

He is a member of COST Action MiMed (TD1301), "Development of a European-based Collaborative Network to Accelerate Technological, Clinical and Commercialisation Progress in the Area of Medical Microwave Imaging", and COST Action TU1208, "Civil Engineering Applications of Ground Penetrating Radar". His research interests include electromagnetic inverse scattering problems for non-invasive diagnostics, ground penetrating radar, compressive sensing, numerical methods for forward scattering problems and biomedical applications of microwave imaging.

Dr. Ambrosanio is a Referee of the IEEE JOURNAL OF SELECTED TOPICS IN APPLIED EARTH OBSERVATIONS and IEEE GEOSCIENCE AND REMOTE SENSING LETTERS.

Panagiotis Kosmas (S'03-M'05-SM'14) received the Diploma in Electrical and Computer Engineering from the National Technical University of Athens, Greece, in 1999, and the M.S. and Ph.D. degrees in Electrical and Computer Engineering from Northeastern University, Boston, MA, in 2002 and 2005, respectively. He joined Kings College London (KCL) in 2008 as a Lecturer, and is currently a Senior Lecturer at KCLs Department of Informatics. Prior to his appointment at KCL, he held research positions at the Center for Subsurface Sensing and Imaging Systems, Boston, USA, the University of Loughborough, UK, and the Computational Electromagnetics Group, University of Wisconsin-Madison, USA. He is also a co-founder of Mediwise Ltd, an award-winning UK-based SME focusing on the use of electromagnetic waves for medical applications. He is an elected Working Group leader for COST Action MiMed (TD1301), "Development of a European-based Collaborative Network to Accelerate Technological, Clinical and Commercialisation Progress in the Area of Medical Microwave Imaging". His research interests include computational electromagnetics with application to sensing and imaging, antenna design, physics-based detection methods, and inverse problems theory and techniques.

Vito Pascazio (SM'11) graduated summa cum laude in electronic engineering from the Universit di Bari, Bari, Italy, in 1986. In 1990, he received the Ph.D. degree in Electronic Engineering and Computer Science from the Department of Electronic Engineering, Universit di Napoli Federico II, Napoli, Italy. In 1990, he was at the Research Institute on Electromagnetics and Electronic Devices (IRECE), Italian National Council of Research (CNR), Napoli, Italy. Currently, he is a Full Professor and Chair of the Department of Engineering at the Università di Napoli Parthenope, Napoli, Italy. From 1994 to 1995, he was a Visiting Scientist at the Laboratoire des Signaux et Systemes of the Ecole Superieure d Electricite (Supelec), Gif sur Yvette, France, and from 1998 to 1999, with the Universite de Nice Sophia-Antipolis, Nice, France. He is also Director of National Laboratory of Multi-Media Communications of the Italian Consortium of Telecommunications (CNIT), Napoli, Italy. He has published more than 170 technical papers. His research interests include fields of remote sensing, and linear and non-linear estimation, with particular emphasis to image computing and processing, and reconstruction of microwave and radar images. Dr. Pascazio was awarded the Philip Morris Prize for Scientific and Technological Research, in 1990. He was a General Co-Chairman of IGARSS-2015 conference.